Microstructural evolution and nanocrystal formation in Pb^+-implanted $ZrSiO_4$ single crystals

Jie Lian
Department of Nuclear Engineering and Radiological Sciences, University of Michigan, Ann Arbor, MI 48109-2104

Susana Ríos
Department of Earth Sciences, University of Cambridge, Downing Street, CB2 3EQ Cambridge, United Kingdom

Lynn A. Boatner
Condensed Matter Sciences Division, Oak Ridge National Laboratory, Oak Ridge, Tennessee 37831-6056

L. M. Wang
Department of Nuclear Engineering and Radiological Sciences, University of Michigan, Ann Arbor, Michigan 48109-2104

Rodney C. Ewing[a)]
Department of Nuclear Engineering and Radiological Sciences; Department of Materials Science and Engineering, University of Michigan, Ann Arbor, MI 48109-2104

(Received 11 June 2003; accepted 25 August 2003)

Single crystals of $ZrSiO_4$ (zircon) with a (110) orientation were implanted with 300 keV Pb^+ at room temperature to fluences ranging from 10^{14} to 10^{17} ions/cm^2. The damage accumulation and microstructural evolution were analyzed by cross-sectional transmission electron microscopy (TEM) and glancing-angle x-ray diffraction (XRD). The experimental damage profiles as observed by TEM and XRD methods were compared to Monte Carlo simulations using the SRIM-2000 code. At the lowest ion fluence (10^{14} ions/cm^2), a buried amorphous layer formed in the zircon matrix. The surface layer is highly damaged and consists of zircon nanocrystals. The critical amorphization dose for zircon implanted with 300 keV Pb^+ was in the range of 0.25–0.43 displacements per atom. With increasing ion fluence, the thickness of the amorphous layer increased. When the Pb concentration in the substrate exceeded ~3.5 at. % (i.e., at 10^{17} ions/cm^2), Pb nanoparticles precipitated at room temperature and formed a layer ~90 nm thick embedded within the amorphous zircon matrix. Effects of the displacement energies employed in the SRIM-2000 simulation on the damage profiles and the critical amorphization dose were also analyzed. © *2003 American Institute of Physics.* [DOI: 10.1063/1.1618917]

I. INTRODUCTION

$ZrSiO_4$ or zircon ($I4_1/amd$, $Z=4$) is extensively utilized in geological age dating and, because of its very high chemical durability, has been proposed as a matrix for the immobilization of plutonium from dismantled nuclear weapons.[1] Natural zircon is commonly found to be in the aperiodic metamict state due to the α decay damage from the radionuclide impurities, ^{238}U, ^{235}U, ^{232}Th, and their decay products.[2–5] The alpha-decay damage causes a dramatic decrease in density (17%) at saturation dose. The refractive indices of zircon, n_c and n_w, decrease with increasing radiation dose to a value of 1.81, at which point the crystal is isotropic. Concurrently, the birefringence decreases from the range of 0.042–0.065 in an undamaged zircon to zero in a completely metamict zircon.[6,7] Ion-beam irradiations have also been used to create buried damage layers of lower refractive index in $ZrSiO_4$ for the purpose of creating optical waveguide regions by either the implanted dopant ions or by the radiation-induced displacive damage.[8,9] Using He^+ ion implantation, Babsail *et al.*[10] synthesized a low-loss optical waveguide by creating a buried amorphous layer with a lower refractive index within a crystalline zircon matrix. Therefore, an understanding of the radiation-induced transformation of zircon from a crystalline-to-amorphous state is important to the nanoscale manipulation of the properties of zircon.

There are extensive studies of radiation effects induced by ''self-radiation'' damage from incorporated actinides in naturally occurring zircons[11–14] or ^{238}Pu-doped zircon.[15–17] The techniques used to characterize the radiation damage and microstructural evolution include: X-ray diffraction (XRD),[11–15] electron microscopy,[4,5,18–20] Raman[7,21,22] and infrared spectroscopy studies.[23–26] With increasing radiation dose (α-decay events), the XRD or electron diffraction intensity characteristic of crystalline zircon gradually diminishes, and amorphous features appear due to the increasing percentage of aperiodic regions until the material reaches a fully amorphous state. Short-range order remains even in the fully amorphous state as shown, for example, by Raman[7,21,22]

a)Electronic mail: rodewing@umich.edu

and infrared spectroscopy studies.[23–26] Although the level of understanding of the nature of the radiation-induced crystalline-to-amorphous transformation in zircon has increased significantly, there are still many aspects that remain unclear. These include the dose dependence of the amorphous fraction, the crystalline-to-amorphous transition mechanism, the structure of amorphous zircon upon radiation damage, and the damage recovery processes over geological time.[27]

Numerous ion-beam irradiation studies[18,20,28–34] have been completed in order to simulate the α-decay damage occurring in actinide-bearing zircons, and the radiation damage and microstructural evolution have been characterized using transmission electron microscopy (TEM). In these studies, both heavy- and light-ion irradiations were performed at controlled temperatures. *In situ* irradiations combined with TEM have been used to observe the microstructural evolution due to ion-beam damage in real time. The critical amorphization dose, D_c, the irradiation dose required to fully amorphize a given material, was determined as a function of temperature. The damage process from ion-beam irradiation is comparable to that in natural zircons subjected to α-decay events, and the critical amorphization dose was found to be independent of the radiation sources and energies.[4] Although ion-beam irradiation reproduces the microstructure of α-decay damaged zircon under controlled temperature conditions, there are a number of experimental limitations. The high surface area to irradiated volume ratio in the electron-transparent region of the sample may affect the damage accumulation process; that is, isolated defects migrate and are annihilated at the surface. The electron beam may cause the radiation-enhanced migration of defects; thus, increasing the dose required for amorphization. These limitations can be overcome by bulk sample irradiations followed by cross-sectional TEM analysis. This provides a direct measurement of the damage distribution, and a detailed microstructural characterization along the trajectory of the implanted ions may be completed. However, a substantial fraction of the amorphous domains (up to 20%) in the crystalline substrate, or residual atomic-scale ordering from embedded nanoparticles in the amorphous matrix may not be evident in the high-resolution TEM image.[35] Thus, TEM techniques cannot provide a reliable quantitative estimate of the amorphous fraction. More sensitive techniques, such as XRD, are needed to characterize the radiation damage and determine the amorphous fraction. Accordingly, in the present study, we have performed bulk sample irradiations of zircon single crystals at room temperature, and the resulting microstructural evolution was characterized by cross-sectional TEM methods combined with glancing-angle XRD. The damage profiles observed by cross-sectional TEM and XRD are compared to Monte Carlo simulations made using the SRIM-2000 code.[36]

II. EXPERIMENT

$ZrSiO_4$ single crystals were synthesized in a Li_2MoO_4 flux that was heated to 1300 °C in a covered Pt crucible and then cooled at 1 °C/h. Crystals with a (110) orientation were mounted for the 300 keV Pb^+ ion implantation that was performed at room temperature with the samples irradiated to fluences of 10^{14}, 10^{15}, 10^{16}, and 10^{17} Pb ions/cm^2. During ion implantation, the ion-beam was aligned ~15° normal to the surface of the (110) face to avoid channeling effects. The radiation damage and implanted microstructures were examined using cross-sectional and high-resolution TEM (HRTEM) techniques with a JEOL JEM 2010F microscope operating at 200 keV. Glancing-incidence XRD was completed using an in-house-designed diffractometer[37] that employed Cu $K\alpha_1$ radiation and a position-sensitive detector covering 120° in 2θ. The incident angle was typically between 0.2°–5°. For comparison purposes, a highly damaged natural zircon was also studied. This sample incorporated 4370±90 ppm of uranium and 1320±200 ppm of thorium and is estimated to be ~85% amorphous.[14]

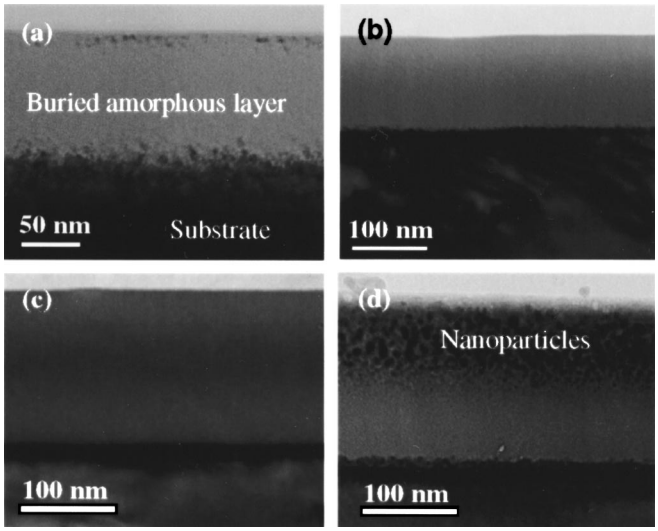

FIG. 1. Cross-sectional TEM images of zircon single crystals implanted with 300 keV Pb^+ at room temperature: (a) 10^{14}, (b) 10^{15}, (c) 10^{16}, and (d) 10^{17} ions/cm^2.

III. RESULTS

The cross-sectional bright-field TEM images of $ZrSiO_4$ implanted by 300 keV Pb^+ at different ion fluences are shown in Fig. 1. At relatively low ion fluence (10^{14} ions/cm^2), a buried amorphous layer was created, and no diffraction contrast was observed within this layer. Highly damaged regions were found at the sample surface and below the buried amorphous layer, as shown by the dark contrast region in the image [Fig. 1(a)]. This highly damaged surface layer becomes fully amorphous at higher fluences (10^{15} ions/cm^2). Further ion implantation thickens the amorphous layer. Based on the cross-sectional TEM images, the thickness of the amorphous layer at ion fluences of 10^{14}, 10^{15}, 10^{16}, and 10^{17} ions/cm^2 can be approximately determined to be ~70, 120, 155, and 178 nm, respectively. Upon ion irradiation at a dose of 10^{17} ions/cm^2, a nanocomposite layer was created, as shown by the strong dark contrast evident in Fig. 1(d). The nanocomposite layer was found to be ~90 nm thick as seen in a higher magnification cross-sectional TEM image [Fig. 2(a)]. The size of the nanopar-

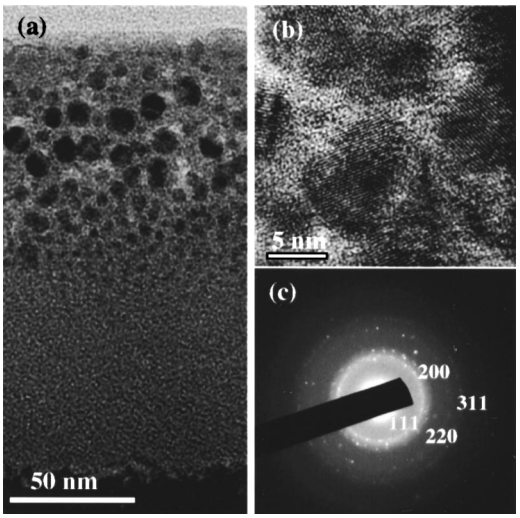

FIG. 2. Higher magnification cross-sectional TEM image (a) of zircon after 10^{17} Pb ions/cm^2 implantation showing the formation of Pb nanocrystals (~90 nm thick layer). The nanoparticles were determined to be fcc Pb by HRTEM images (b) and selected area diffraction patterns (c).

ticles ranged from several nm to ~10 nm with an average value of ~6 nm. Energy dispersive spectroscopy (EDS) of the nanoparticles gives strong signals characteristic of Pb. Both HRTEM images [Fig. 2(b)] and selected-area electron diffraction patterns [Fig. 2(c)] can be indexed from the crystallographic data of face-centered-cubic (fcc) Pb, indicating that nanosized Pb-particles precipitated in the amorphous zircon matrix.

The increasing thickness of the damaged layer with increasing ion fluence and the formation of Pb precipitates in the sample irradiated with 10^{17} ions/cm^2 were also observed by glancing-angle XRD. Figure 3 shows the diffractograms obtained for three of the implanted $ZrSiO_4$ samples at an incident angle of 1.5° after having subtracted the background caused by air-related scattering. In samples irradiated with 10^{15} and 10^{16} ions/cm^2, only the signal coming from the amorphous zircon layer was observed. During the XRD examination, the sample orientation was chosen to minimize

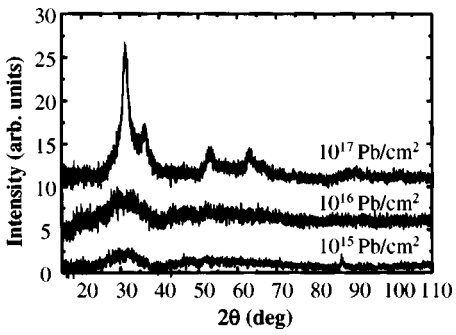

FIG. 3. Diffractograms obtained under identical experimental conditions (1.5° incident angle) for $ZrSiO_4$ samples implanted with increasing Pb^+ fluence. Diffractograms have been offset for clarity. For samples irradiated with 10^{15} and 10^{16} Pb ions/cm^2, the surface is totally damaged and the characteristic pattern of amorphous zircon can be observed. The sharp Bragg peak in sample irradiated at 10^{15} Pb ions/cm^2 comes from the undamaged bulk zircon. For a sample irradiated at 10^{17} Pb ions/cm^2, diffraction maxima from precipitated Pb nanoparticles are found.

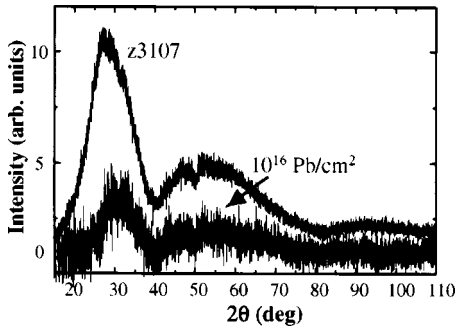

FIG. 4. Diffractograms corresponding to an implanted $ZrSiO_4$ sample and a natural sample containing ~85% of amorphous regions. For comparison purposes, the diffractogram for a natural zircon sample has been normalized by a factor of 3.

diffraction maxima from the bulk $ZrSiO_4$. The intensity in the sample irradiated with 10^{14} ions/cm^2 was too weak to be extracted from the background. As shown in Fig. 4, the pattern found for the implanted samples is similar to that found in highly damaged natural zircon.[14] The intensity in natural zircon is approximately one order of magnitude stronger. This is due to the fact that, although measurements were performed under exactly the same conditions, the damaged region in the ion-implanted sample is restricted to a thin layer; whereas, the natural sample is damaged throughout its entire volume. The slight asymmetry of the first peak in the natural zircon sample arises from the contribution of the (200) diffraction maximum coming from crystalline ''islands'' remaining in the amorphous matrix.

In order to determine the thickness of the damaged layer in the implanted samples, we compared the signal obtained from implanted and natural samples by the following method: Given the absorption coefficient of damaged zircon, 376 cm^{-1},[38] and the incident angle of 1.5°, the penetration depth of the copper $K\alpha_1$ radiation was found to be ~1.39 μm.[39] Using the integrated intensity over the whole 2θ range, we normalized the data obtained for the implanted samples with the data obtained in the natural sample. For the case of the sample irradiated with 10^{17} ions/cm^2, the peak intensity coming from Pb-nanoparticles was first subtracted [see Fig. 5(a)]. Figure 6 compares the thickness of the amorphous layer obtained by XRD with the values obtained by cross-sectional TEM. Despite the large error bars for the XRD results, the agreement is good.

As the incident angle, α_i, increases, the beam penetrates further into the sample, and therefore, the contribution from the damaged region decreases. For the case of the sample irradiated with 10^{17} ions/cm^2, this means that diffraction maxima coming from the embedded Pb-nanoparticles become weaker, see Fig. 5(b). Figure 7 shows the behavior of the integrated intensity of the doublet (111)/(200) as a function of the incident angle. The peak profile was fitted to three Gaussian functions [see Fig. 5(a)], and the contribution from the amorphous layer was subsequently subtracted. The full width at half maximum for the peaks (111)/(200) was found to be 1.54(1)° (the instrumental resolution was 0.09°). Using Scherrer's equation,[40] the mean size of the Pb-particles was, therefore, estimated to be ~6 nm in good agreement with the

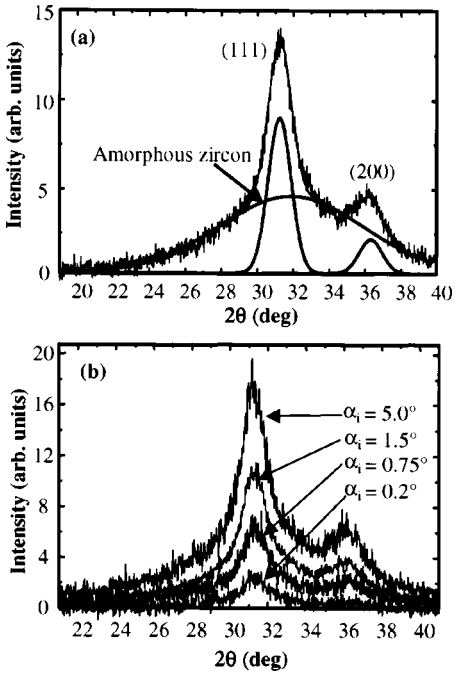

FIG. 5. (a) Intensity of the (111)/(200) Pb peaks in the sample irradiated at 10^{17} Pb ions/cm^2 for an incident angle of 0.5°. Note the contribution due to the amorphous zircon layer. (b) Intensity of the (111)/(200) Pb peaks as a function of the incident angle, α_i.

TEM images. From the data depicted in Fig. 7, and using well-known mathematical expressions,[41] one can extract the thickness of the Pb-containing layer. The continuous line in Fig. 7 is the best fit to the data leading to a thickness of 57 ± 2 nm (an absorption coefficient of 2607 cm^{-1} was used).[38] The thickness of the Pb layer found by XRD (~57 nm) is smaller than that found by TEM (~90 nm). The discrepancy comes from the fact that in the XRD analysis, the pattern is heavily weighted toward the large grains. Moreover, the contribution of the small grains [present below the layer containing the large grains, see Fig. 2(a)] to the XRD pattern is located in the tails of the diffraction maxima. In this case, the contribution of small grains overlaps with the contribution from the amorphous layer, and therefore, is difficult to evaluate.

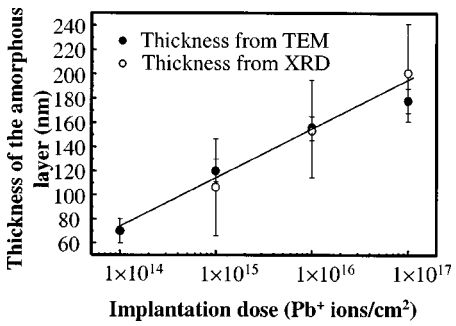

FIG. 6. Thickness of the amorphous $ZrSiO_4$ layer as a function of Pb^+ fluence.

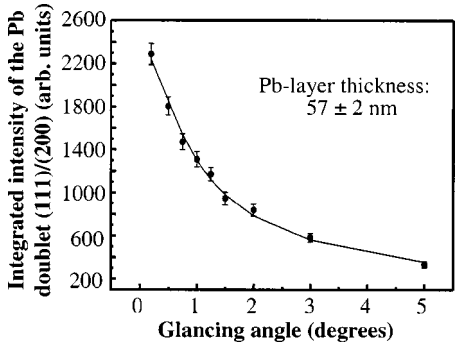

FIG. 7. Intensity of the Pb doublets (111)/(200) (after subtracting the contribution from amorphous $ZrSiO_4$) as a function of α_i. The continuous line is the best fit to the data giving a thickness of ~57 nm.

IV. DISCUSSION

A. Amorphization process

The amorphization process in α-decay-damaged natural zircon involves three different stages with increasing dose—depending on the age of the sample and the concentration of radionuclides. At low damage levels, the α-recoil nuclei produce a few isolated 2–5 nm amorphous regions that give a mottled diffraction contrast in the TEM images. Sharp diffraction maxima are observed in the diffraction pattern, and the material shows a well-defined atomic-scale periodicity. With increasing α-decay dose, areas with a mottled diffraction contrast become more numerous and interconnected, and the microstructure consists of crystalline islands in an aperiodic matrix. During the final stage of radiation damage, zircon appears to be fully aperiodic.

The microstructural evolution of synthetic zircons with increasing dose under various ion irradiations, including 700 and 1500 keV Kr^+, 1500 keV Xe^+, and 400 keV He^+,[28] is comparable in many respects to that of natural zircons.[4,5] A relatively complete picture of the microstructural evolution with increasing radiation dose can be clearly seen from the ion irradiation of bulk samples and subsequent cross-sectional TEM examinations. Figures 8(a) and 8(b) show HRTEM images of the surface layer and the interface between the crystalline and amorphous layers, respectively, for the sample irradiated with 10^{14} Pb ions/cm^2. The buried amorphous layer is further evidenced by the complete loss of lattice fringes when the damage level is above the critical amorphization dose, D_c. At the surface layer, the remaining nanosized $ZrSiO_4$ particles have an orientation similar to that of the crystalline substrate. This suggests that the damage level is below D_c. Strain fields and mottled zones that are indicated by the dark contrast in Fig. 8(b) exist at the crystalline–amorphous interface and in the deeper crystalline regions where the damage level may be less than D_c. HRTEM images of both the surface layer and the crystalline–amorphous interface reveal the existence of amorphous regions that are embedded in the crystalline matrix. This suggests that the amorphization process induced by 300 keV Pb^+ in $ZrSiO_4$ occurs through a heterogeneous displacement process instead of a homogeneous process in which a gradual increase of the point-defect concentration

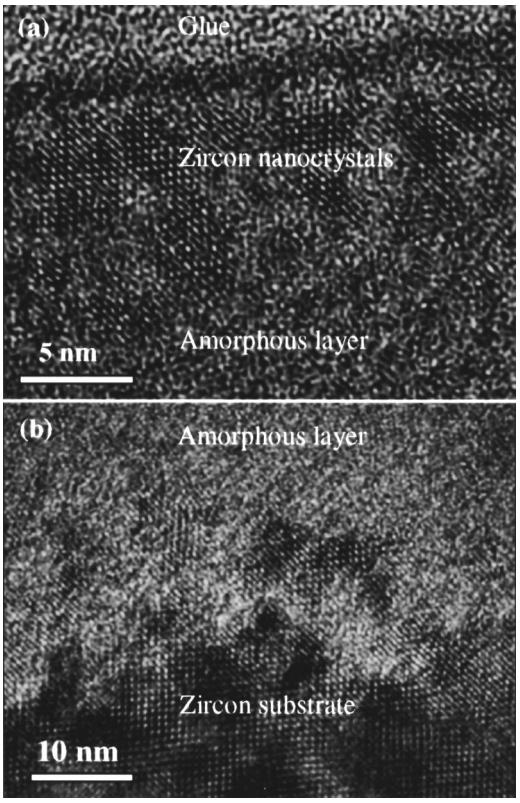

FIG. 8. High-resolution TEM images of the surface layer (a) and the crystalline–amorphous interface (b) of $ZrSiO_4$ implanted with 300 keV Pb^+ to a fluence of 10^{14} ions/cm^2.

leads to a sudden change from a perfectly crystalline to an aperiodic material at a critical defect concentration. These results confirm previous XRD results. According to Ríos *et al.*,[14] the amorphization process in natural zircon occurs as a consequence of the direct impact within cascades caused by α-recoil nuclei, and even at low doses, isolated amorphous zones exist that are the source of the observed diffuse x-ray scattering.

B. TRIM calculations and critical amorphization dose

For ion-beam irradiation studies, Monte Carlo calculations using the TRIM (Transport of Ions in Matter) code are widely used to simulate the damage profile, the distribution of implanted ions, and to convert the damage level to displacements per atom (dpa). The critical amorphization dose for 300 keV Pb^+ implanted in $ZrSiO_4$ crystals can, therefore, be determined by comparing the experimental damage profile with the simulated profile using the SRIM-2000 code. One of the fundamental parameters affecting radiation damage in a material is the threshold displacement energy, E_d, which is the minimum kinetic energy necessary to displace an atom from its equilibrium lattice site. The parameter E_d is essential for quantifying an irradiation dose in terms of the number of displaced atoms in the irradiated material, which allows quantitative comparisons to be made of α-decay damage versus ion-beam-irradiation damage. However, at the present time, no displacement energy for the zircon structure has been determined experimentally. In TRIM simulations, a default value of $E_d = 25$ eV has been used previously for the damage calculation in zircon.[4] Various theoretical methods, such as static energy minimization[42,43] and molecular dynamic simulations,[44,45] have been employed to determine the threshold displacement energies in zircon. These results are summarized in Table I.[27] A significant discrepancy between these simulated threshold displacement energies can be found, especially for Si and O. A critical issue for the quantitative comparison of radiation damage among various α-decay and ion-beam-irradiation studies is, therefore, to use a consistent value for threshold displacement energies in the TRIM simulations.

TABLE I. Calculated threshold displacement energies in zircon.[a]

Method	Zr (eV)	Si (eV)	O (eV)	Reference
Energy minimization	80	20	45	Williford *et al.* (Ref. 42)
Energy minimization	76	85	38	Meis (Ref. 43)
Molecular dynamics	90	98	32	Crocombette and Ghaleb (Ref. 44)
Molecular dynamics	60	48	23	Park *et al.* (Ref. 45)

[a]See Ref. 27.

Room-temperature irradiations of single crystals of zircon with 1.5 MeV Xe^+, 0.7 MeV Kr^+, 1.5 MeV Kr^+, 1.5 MeV Ar^+, 0.8 MeV Ne^+, 0.54 MeV Pb^+, and 0.6 MeV Bi^+ ions have been performed in order to investigate energy density effects (eV/nm/ion) on the amorphization dose.[4,46] Complete amorphization occurred for all of the ions and energies. The critical amorphization dose for single-crystal $ZrSiO_4$ was determined to be ~0.55 dpa.[4] Also, for polycrystalline Pu-doped zircon, the amorphization dose is ~0.59 dpa (this dose calculation included only the 92 keV U^+ recoil-nucleus contribution).[4] These results show that the amorphization dose under high dose rates ($\sim 10^{-4}$ to 10^{-3} dpa/s) for heavy-ion irradiation is nearly identical to that of Pu-doped zircon (3×10^{-9} dpa/s),[15] suggesting that the amorphization process in zircon is independent of the damage source and dose rate. Weber *et al.*[46] recalculated the amorphization dose from various ion-beam irradiations in synthetic zircons, as well as α-decay damage in Pu-doped and natural zircons, using full-cascade TRIM-96 simulations with displacement energies of 80, 20, and 45 eV for Zr, Si, and O (by Williford *et al.*,[42] see Table I), respectively. For this case, the amorphization dose increases with ion mass, more specifically, with increasing damage-energy density, and different amorphization doses were obtained for different ion-beam irradiations—inconsistent with those calculated previously using $E_d = 25$ eV. For example, for 1.5 MeV Kr^+ ion irradiation, the critical amorphization dose can be as low as 0.30 dpa. For 540 keV Pb^+ irradiation in the bulk sample at 77 K, the critical amorphization dose is close to ~0.4 dpa as analyzed by the Rutherford backscattering (RBS) technique. Based on these results, a higher critical amorphization dose was expected for the Pb^+ ion irradiation at room temperature in this study, as compared with that of 540 keV Pb^+ irradiation at 77 K.[46]

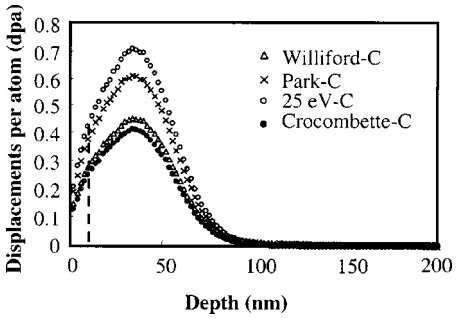

FIG. 9. Full-cascade calculated damage profiles of zircon at a fluence of 10^{14} Pb ions/cm^2 using the SRIM-2000 code with different threshold displacement energies. The critical amorphous dose of zircon subjected to 300 keV Pb^+ implantation can be determined by comparing the experimental microstructure with the calculated damage profiles, as shown by the dotted line at 10 nm depth at which complete amorphization occurred [Fig. 8(a)]. The theoretical density of crystalline zircon was used in the SRIM simulations, as labeled by C.

We performed full-cascade calculations using the SRIM-2000 code using the threshold displacement energies summarized in Table I and the default value of $E_d = 25$ eV. Figure 9 shows the damage profiles for 300 keV Pb^+-implanted $ZrSiO_4$ at a fluence of 10^{14} Pb ions/cm^2. The displacement energies employed in the TRIM simulations have a significant effect on the calculated amorphization dose. As shown in Fig. 8(a), complete amorphization of $ZrSiO_4$ subjected to 10^{14} Pb ions/cm^2 occurred 8–10 nm below the surface layer. By comparing the experimental damage profile [Fig. 8(a)] with the simulated profiles (Fig. 9), the amorphization dose can be precisely determined to be in the range of 0.25–0.43 dpa (see Table II), by varying the threshold displacement energies employed in the TRIM calculations. A significantly lower amorphization dose (as compared with that for *in situ* ion-beam irradiation of $ZrSiO_4$) has been observed in the bulk sample irradiations followed by cross-sectional TEM examination. For example, using 25 eV as the displacement energy, the amorphization dose for 300 keV Pb^+ implantation is 0.39–0.43 dpa, which is lower than that of synthetic zircon subjected to various ion-beam sources with *in situ* TEM observation (~0.55 dpa). Similarly, using the displacement energies of Williford *et al.*,[42] the amorphization dose is 0.25–0.27 dpa, which is lower than that of 0.54 MeV Pb^+-implanted zircon at 77 K (~0.4 dpa). Bulk sample irradiation avoids high-surface-area to irradiated volume ratio and electron-beam radiation-enhanced annealing effects that may lead to the migration and annihilation of isolated defects at the surface. Therefore, the amorphization dose determined from bulk irradiations is expected to be more precise in describing the susceptibility of the material to ion-beam irradiation-induced amorphization than the previous studies that used ion irradiations of thin TEM samples combined with *in situ* TEM characterization.

C. Ion-bombardment-enhanced growth of the amorphous layer

As shown in Fig. 6, the thickness of the amorphous layer resulting from Pb^+ ion bombardment increases with increasing ion fluence. This ion-bombardment-enhanced growth of the amorphous layer has been reported in previous studies.[47–50] Figure 10 shows the damage profile and implanted Pb^+-ion distributions in crystalline $ZrSiO_4$ at various ion fluences using full-cascade SRIM-2000 calculations and Williford's threshold displacement energies.[42] The calculated ion range and damage events corresponding to different displacement energies are summarized in Table II. For the 300 keV Pb^+ implantation, the ion range is less sensitive to displacement energies than the amorphization dose. Also, the calculated approximate ion range (53.4±14.7 nm) is deeper than the damage peak (~38 nm), but much less than the observed damage depth at all ion fluences. This discrepancy between calculated damage profile and experimental microstructure can be explained by detailed calculations of ion and recoil distributions. The damage in the region below the Pb^+ range can be mainly attributed to the displacements caused by O, Si, and Zr recoils, which can penetrate deeper into the $ZrSiO_4$ crystalline matrix than the Pb^+ ions because of their smaller atomic masses and lower stopping powers. The inset in Fig. 11 shows the penetration depth for O, Si, and Zr recoils and Pb^+ ions at the end of the ion range.

The accumulated damage level increases with increasing ion fluences at all depths across the cross-sectional damage profile, as evidenced in Fig. 10(b). Using ~0.25 dpa as the critical amorphization dose (using threshold displacement energies by Williford *et al.*,[42] see Table II), the thickness of the amorphous layer can be determined to be 50, 88, 118, and 156 nm, respectively, for 10^{14}, 10^{15}, 10^{16}, and

TABLE II. Damage profiles and ion ranges of zircon implanted with 300 keV Pb^+ by full-cascade calculation using the SRIM-2000 code[a] with the densities of crystalline and amorphous zircon of ~4.7 g/cm^3 and ~3.9 g/cm^3, respectively.

Displacement energies in zircon	Ion range (nm)		Critical amorphization dose D_c (dpa)		Amorphous layer thickness (nm) at $10^{14}/10^{15}/10^{16}/10^{17}$ ions/cm^2	
	crystalline	amorphous	crystalline	amorphous	crystalline	amorphous
Williford *et al.* (Ref. 42)	53.4±14.7	64.2±17.7	0.25–0.27	0.23–0.25	50/86/118/156	66/104/144/184
Crocombette and Ghaleb (Ref. 44)	53.4±14.7	64.3±17.7	0.235–0.257	0.216–0.235	52/86/116/154	66/104/146/188
Park *et al.* (Ref. 45)	53.4±14.7	64.3±17.7	0.34–0.37	0.31–0.338	52/86/118/154	66/104/142/182
25 eV	53.4±14.7	64.3±17.7	0.39–0.43	0.36–0.39	52/86/118/156	66/104/144/186

[a]See Ref. 36.

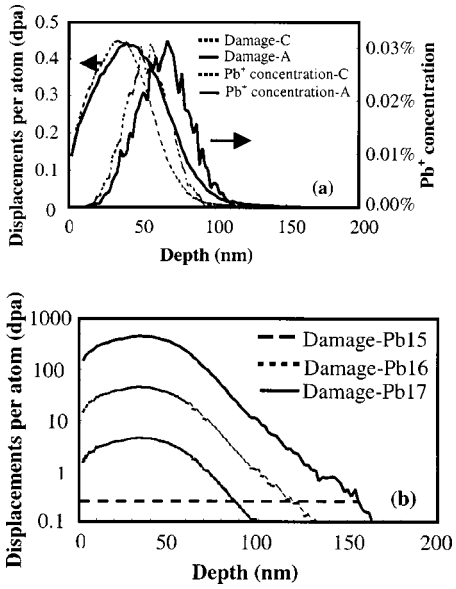

FIG. 10. (a) Damage profiles and ion concentrations of Pb^+ (at 10^{14} Pb ions/cm^2) in the crystalline zircon matrix determined by full-cascade calculations using SRIM-2000 with the threshold displacement energy determined by Williford *et al.* (see Ref. 42) (see Table I). For comparison, the calculated damage profile and the Pb^+-ion distribution calculated by SRIM-2000 using the density of amorphous zircon ($\sim$3.9 g/cm^3) are included in (A). (b) Damage profiles of 300 keV Pb^+ in crystalline zircon ($\sim$4.7 g/cm^3) at 10^{15}, 10^{16}, and 10^{17} Pb ions/cm^2 with the threshold displacement energy by Williford *et al.* (see Ref. 42). Using 0.25 dpa as the critical amorphous dose, the thickness of the amorphous layer at different ion fluences can be determined, as indicated by the intercept of the dotted line with the different curves.

10^{17} Pb ions/cm^2 [see Fig. 10(b)]. Therefore, the ion-bombardment-induced increase in the amorphous zone can be explained by increasing damage levels with increasing ion fluence. However, there are still significant discrepancies between the calculated amorphous layer thickness and the observed microstructure. For $ZrSiO_4$ crystals, there is a significant density decrease with increasing α-decay dose and ion-beam radiation damage[5,12] due to the volume swelling of amorphous zircon. Depending on the degree of damage, the swelling of amorphous domains may vary from $\sim$0% for lower doses (below 2×10^{18} α-decays/g) to a maximum value of $\sim$18% (above 8×10^{18} α-decays/g).[14] Correspondingly, the density decreased by 17% (from $\sim$4.7 to 3.90 g/cm^3 at a dose of 10^{19} α-decays/g). Weber[15] also reported

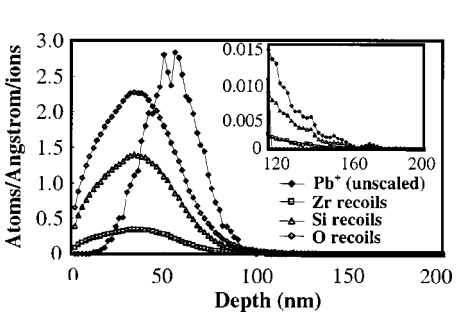

FIG. 11. Calculated ion and recoil distributions in the crystalline zircon matrix implanted with 300 keV Pb^+ by full-cascade SRIM simulation with the threshold displacement energies of Williford *et al.* (see Ref. 42). The inset shows the end of the ion/recoil range at a larger scale.

that the overall density of Pu-doped synthetic zircon decreased by 16% before reaching a saturation value. We recalculated the damage profile using SRIM-2000 assuming a density of 3.9 g/cm^3 for amorphous zircon at all ion fluences. As shown in Fig. 10(a) and Table II, both the damage profile and Pb^+-ion range in an amorphous zircon matrix shift to a depth greater than those in the crystalline zircon matrix. The thickness of the amorphous layer can be determined to be approximately 66, 104, 144, and 184 nm for 10^{14}, 10^{15}, 10^{16} and 10^{17} ions/cm^2, respectively. Considering the dimensional change caused by volume swelling of amorphous zircon due to implanted Pb^+ ions, the damage range predicted by TRIM simulations is close to the experimental damage profiles as observed by cross-sectional TEM and by XRD.

D. Pb precipitation and nanoparticle formation

Ion-implantation techniques have been used extensively in creating nanocomposite materials and nanostructures.[51] As shown in Fig. 2(a), a nanocomposite layer was formed by 300 keV Pb^+-ion implantation in zircon at room temperature at a fluence of 10^{17} Pb ions/cm^2. Nanoparticles with the largest sizes are distributed at a depth of 20–60 nm. This nanoparticle formation may be attributed to a solid-state supersaturation caused by high-ion-dose implantation at a depth where the implanted ion concentration is greater than its solubility in the matrix. The Pb nanocrystal formation in a $ZrSiO_4$ matrix is further evidenced by a *z*-contrast image obtained with high-angle annual dark-field scanning TEM (HAADF-STEM) [Fig. 12(a)]. At a lower ion fluence (10^{16} Pb ions/cm^2), no evidence of nanocrystal formation was found [Figs. 1(c) and 12(b)]. The brighter contrast in the HAADF images [Figs. 12(a) and 12(b)] is attributed to the heavier atomic mass of Pb. STEM-energy dispersive x-ray scanning along the white line in Fig. 12(b) indicates a Gaussian distribution of Pb^+ ions [Fig. 12(c)] with a peak concentration of $\sim$3 at. % at a depth of $\sim$76 nm, close to the ion range ($\sim$64.2$\pm$17.7 nm). Figure 13 compares the Pb^+-ion distributions for 10^{16} and 10^{17} Pb ions/cm^2 using the displacement energy of Williford *et al.*[42] For 10^{16} Pb ions/cm^2, the peak ion concentration is estimated to be $\sim$3.1 at. % (Fig. 13), consistent with the STEM-energy dispersive spectroscopy (EDS) measurement [Fig. 12(c)]. However, although the maximum Pb^+ level at 10^{17} Pb ions/cm^2 is at $\sim$64 nm (Fig. 13), the largest Pb nanoparticles are at a depth of $\sim$50 nm [Fig. 12(a)]. This suggests that once a critical concentration of Pb^+ is reached, additional implanted Pb^+ does not penetrate deeply; thus, the Pb nanoparticles form at a shallower depth. From the present results, a rough estimate indicates that Pb nanoparticles are expected to precipitate in amorphized zircon when the Pb^+ concentration exceeds $\sim$3.5 at. %.

There is some concern that the implanted Pb^+ might be redistributed either by the subsequent incident ions or by diffusion to the surface. A very slow diffusivity of Pb in crystalline zircon has been reported over the temperature range of 1000–1500 °C,[52] while a faster transport of Pb was found in metamict zircon because the high defect concentration may enhance the diffusivity.[53] A RBS spectroscopy

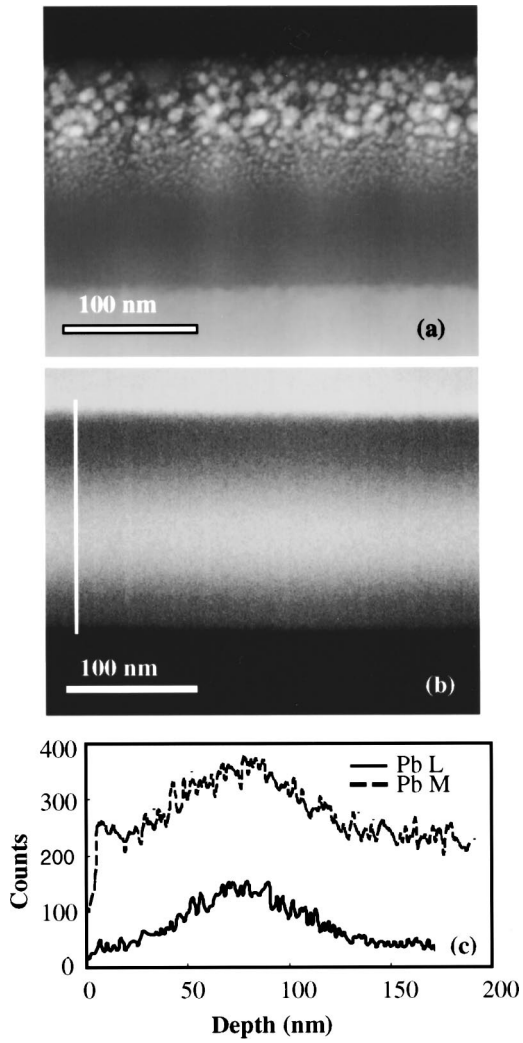

FIG. 12. HAADF-STEM images showing the formation of Pb nanoparticles (10^{17} Pb ions/cm^2) (a), and the Pb^+ elemental distribution in implanted zircon matrix (10^{16} ions/cm^2) (b). (c) Pb^+ profile in a $ZrSiO_4$ matrix obtained by STEM-EDS scanning along the white line in (b).

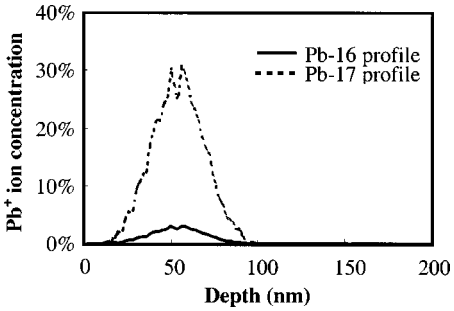

FIG. 13. Pb^+ ion concentrations in amorphous zircon implanted at fluences of 10^{16} and 10^{17} Pb ions/cm^2 using a SRIM-2000 full calculation with the displacement energies of Williford *et al.* (see Ref. 42). The peak level of the Pb^+ concentration (10^{16} Pb ions/cm^2) is ~3.1 at. %, consistent with the STEM-EDS line scanning [Fig. 12(c)]. No evidence of nanocrystallization was found, suggesting that ~3.1 at. % Pb^+ may be incorporated into the amorphous domains of zircon.

study of zircon single crystals implanted by 100 keV Pb^+ to a fluence of 10^{15} ions/cm^2 at room temperature revealed no significant redistribution of the near-surface elements as a result of the ion implantation.[54]

Thus, one important parameter related to the fcc Pb nanoparticle precipitation is the solubility of Pb^+ ions in amorphous $ZrSiO_4$. Although pertinent experimental data are not available, studies[52,55] have been completed in order to understand the equilibrium and kinetic behavior of both the parent (U,Th) and daughter (Pb) elements in the crystalline zircon structure because of the importance of zircon in U–Th–Pb age dating. Generally, lead ($Pb^0 = 0.174$ nm and $Pb^{2+} = 0.129$ nm) is not easily accommodated in the Zr-site of the zircon structure due to its larger ionic radius and the difference in charge ($Zr^{4+} = 0.084$ nm). Only Pb^{4+} (0.094 nm, eight coordination) has an ionic radius[56] and charge that is compatible with substitution for Zr^{4+} (0.084 nm). As a result, natural zircon tends to reject Pb during the crystal growth process, and most Pb in natural zircon is produced *in situ* from U and Th decay. However, small amounts of nonradiogenic Pb (~2 ppb to 80 ppm) can exist in natural zircons as impurities.[57]

Watson *et al.*[55] studied the incorporation of Pb in the crystalline zircon structure by synthesizing zircon crystals using different approaches including: a high-temperature growth of large crystals from Pb-silicate melts, hydrothermal coating of thin epitaxial layers on natural zircon substrates, and the growth of small homogeneously nucleated crystals from aqueous fluids. In a P_2O_5-free system, zircon contained <1 ppm Pb, despite 66 wt % PbO in the melt, and with the addition of 5 wt % P_2O_5 to the melt, ~1500 ppm Pb can be incorporated into zircon structure due to a specific charge-balance mechanism: $[2P^{5+} + Pb^{2+}] = [2Si^{4+} + Zr^{4+}]$.[55,58] A high concentration of nonradiogenic Pb (>3 at. %) can be incorporated in fluid-grown low-temperature zircons prepared by hydrothermal overcoating methods with the zircon/fluid partition coefficients of 4.2 and 2.6 for Pb^{4+} and Pb^{2+}, respectively. The charge balance is compensated by H^+. Because of the rapid, polythermal modes of zircon growth and extremely Pb-rich environments in the experimental systems, the high Pb compatibility under these growth circumstances may not be an equilibrium state. Limited knowledge exists about the incorporation of Pb into amorphous or metamict zircon.

A higher Pb compatibility in amorphous zircon is expected because of the damaged structure, which may enhance the Pb diffusivity. The degree of U–Pb isotopic discordance (Pb loss) correlated closely with the degree of metamictization of single zircon grains.[59] Most Pb loss in zircon is likely a consequence of recrystallization or Pb transport in zircons with severe radiation damage.[52] Metamictization enhances the relative potential for the radiogenic loss of Pb in zircon.[59] In this study, we have shown that Pb^+ with ion concentrations slightly above ~3.1 at. % (see Fig. 13) are quite compatible with the amorphous zircon structure, comparable to the large amount (>3 at. %) of Pb in crystalline zircon synthesized under hydrothermal conditions.[55] No precipitation of Pb was observed in the sample implanted by Pb^+ at a fluence of 10^{16} ions/cm^2.

V. CONCLUSIONS

Single-crystal zircon has been implanted by 300 keV Pb^+ to fluences of 10^{14}, 10^{15}, 10^{16}, and 10^{17} Pb ions/cm^2, and the radiation damage and microstructural evolution upon ion implantation have been characterized by cross-sectional TEM and glancing-angle XRD methods. At low-ion-fluence implantation (10^{14} Pb ions/cm^2), the complete amorphization process of zircon was studied using cross-sectional TEM observations that included the buried amorphous layer, crystalline domains in the amorphous matrix, and the ''mottled'' zone in the crystalline substrate. Both cross-sectional TEM and glancing-angle XRD results indicated that the increasing ion fluences thicken the amorphous zone. The experimental microstructure was compared with calculated damage profiles and ion distributions using SRIM-2000 simulations. From SRIM simulations, the critical amorphization dose is in the range of 0.25–0.43 dpa, which is significantly lower than the ion-irradiation damage found under *in situ* TEM observation conditions. Pb nanoparticles precipitated at room temperature from the amorphous zircon matrix when the Pb-ion concentration exceeded ~3.5 at. % (i.e., at 10^{17} ions/cm^2.)

ACKNOWLEDGMENTS

This work was supported by the Division of Materials Science of the Office of Basic Energy Science of the U.S. DOE [Grant No. DE-FG02-97ER45656 to one of the authors (R.C.E.)] and the Natural Environment Research Council of the U.K. for another author (SR). This research was sponsored in part by the Laboratory Directed Research and Development Program of Oak Ridge National Laboratory. Oak Ridge National Laboratory is managed by UT-Battelle, LLC, for the U.S. Dept. of Energy under Contract No. DE-AC05-00OR22725. The JEOL-2010F STEM/TEM used in this study was funded by NSF through the Grant No. DMR-9871177 and is operated by the Electron Microscopy Analysis Laboratory at University of Michigan.

[1] R. C. Ewing, W. Lutze, and W. J. Weber, J. Mater. Res. **10**, 243 (1995).
[2] R. C. Ewing, Nucl. Instrum. Methods Phys. Res. B **91**, 22 (1994).
[3] G. R. Lumpkin and R. C. Ewing, Phys. Chem. Miner. **16**, 2 (1988).
[4] W. J. Weber, R. C. Ewing, and L. M. Wang, J. Mater. Res. **9**, 688 (1994).
[5] T. Murakami, B. C. Chakoumakos, R. C. Ewing, G. R. Lumpkin, and W. J. Weber, Am. Mineral. **76**, 1510 (1991).
[6] M. Stackelberg and E. Rottenbach, Z. Kristallogr. **97**, 173 (1940).
[7] C. S. Palenik, L. Nasdala, and R. C. Ewing, Am. Mineral. **88**, 770 (2003).
[8] P. D. Townsend, Nucl. Instrum. Methods Phys. Res. B **65**, 243 (1992).
[9] K. Wenzlik, J. Heibei, and E. Voges, Phys. Status Solidi A **61**, K207 (1980).
[10] L. Babsail, N. Hamelin, and P. D. Townsend, Nucl. Instrum. Methods Phys. Res. B **59**, 1219 (1991).
[11] H. D. Holland and D. Gottfried, Acta Crystallogr. **8**, 291 (1955).
[12] S. Ríos and E. K. H. Salje, J. Phys.: Condens. Matter **11**, 8947 (1999).
[13] E. K. H. Salje, J. Chrosch, and R. C. Ewing, Am. Mineral. **84**, 1107 (1999).
[14] S. Ríos, E. K. H. Salje, M. Zhang, and R. C. Ewing, J. Phys.: Condens. Matter **12**, 2401 (2000).
[15] W. J. Weber, J. Mater. Res. **5**, 2687 (1990).
[16] W. J. Weber, Radiat Eff. Defect **115**, 341 (1991).
[17] W. J. Weber, R. C. Ewing, and A. Meldrum, J. Nucl. Mater. **250**, 147 (1997).
[18] A. Meldrum, S. J. Zinkle, L. A. Boatner, and R. C. Ewing, Nature (London) **395**, 56 (1998).
[19] L. A. Bursill and A. C. McLaren, Phys. Status Solidi **13**, 331 (1966).
[20] K. Yada, T. Takayoshi, and I. Sunagawa, Phys. Chem. Miner. **7**, 47 (1981).
[21] L. Nasdala, G. Irmer, and D. Wolf, Eur. J. Mineral **7**, 471 (1995).
[22] M. Zhang, E. K. H. Salje, I. Farnan, A. Graeme-Barber, P. Daniel, R. C. Ewing, A. M. Clark, and H. Leroux, J. Phys.: Condens. Matter **12**, 1915 (2000).
[23] J. A. Woodhead, G. R. Rossman, and L. T. Silver, Am. Mineral. **76**, 74 (1991).
[24] M. Zhang, E. K. H. Salje, and R. C. Ewing, J. Phys.: Condens. Matter **15**, 3445 (2003).
[25] M. Zhang and E. K. H. Salje, J. Phys.: Condens. Matter **13**, 3057 (2001).
[26] M. Zhang, E. K. H. Salje, R. C. Ewing, I. Farnan, S. Ríos, Schlüter, and P. Leggo, J. Phys.: Condens. Matter **12**, 5189 (2000).
[27] R. C. Ewing, A. Meldrum, L. M. Wang, W. J. Weber, and L. R. Corrales *Radiation Effects in Ziron*, Reviews in Mineralogy and Geochemistry edited by J. M. Hanchar, and P. W. O. Haskin, (Mineralogy Society of America, 2003) (in press).
[28] L. M. Wang and R. C. Ewing, MRS Bull. **17**, 38 (1992).
[29] A. Meldrum, L. A. Boatner, and R. C. Ewing, Phys. Rev. B **56**, 13805 (1997).
[30] A. Meldrum, L. A. Boatner, W. J. Weber, and R. C. Ewing, Geochim. Cosmochim. Acta **62**, 2509 (1998).
[31] A. Meldrum, L. M. Wang, and R. C. Ewing, Nucl. Instrum. Methods Phys. Res. B **116**, 220 (1996).
[32] A. Meldrum, S. J. Zinkle, L. A. Boatner, and R. C. Ewing, Phys. Rev. B **59**, 3981 (1999).
[33] R. C. Ewing, A. Meldrum, L. M. Wang, and S. X. Wang, Rev. Mineral. Geochem. **39**, 319 (2000).
[34] L. M. Wang and R. C. Ewing, Nucl. Instrum. Methods Phys. Res. B **65**, 319 (1992).
[35] M. L. Miller and R. C. Ewing, Ultramicroscopy **48**, 203 (1992).
[36] J. F. Ziegler (2002) http://www.SRIM.org/.
[37] K. R. Locherer, S. A. Hayward, P. J. Hirst, J. Chrosch, M. Yeadon, J. S. Abell, and E. K. H. Salje, Philos. Trans. R. Soc. London, Ser. A **354**, 2815 (1996).
[38] J. H. Hubbell and S. M. Seltzer, *Tables of X-Ray Mass Attenuation Coefficients and Mass Energy—Absorption Coefficients*, Version 1.03 (National Institute of Standards and Technology, Gaithersburg, MD, 1997).
[39] J. S. Rigden, R. J. Newport, and G. Bushnell-Wye, J. Mater. Res. **12**, 264 (1997).
[40] B. E. Warren, *X-ray Diffraction* (Addison–Wesley, Reading, MA, 1969).
[41] B. D. Cullity, *Elements of X-ray Diffraction*, 2nd Ed (Addison–Wesley, Reading, MA, 1978).
[42] R. E. Williford, R. Devanathan, and W. J. Weber, Nucl. Instrum. Methods Phys. Res. B **141**, 94 (1998).
[43] C. Meis and R. C. Ewing (personal communication).
[44] J. P. Crocombette and D. Ghaleb, J. Nucl. Mater. **295**, 167 (2001).
[45] B. Park, W. J. Weber, and L. R. Corrales, Phys. Rev. B **64**, 174108 (2001).
[46] W. J. Weber, R. Devanathan, A. Meldrum, L. A. Boatner, R. C. Ewing, and L. M. Wang, Mater. Res. Soc. Symp. Proc. **540**, 367 (1999).
[47] W. L. Gong, L. M. Wang, and R. C. Ewing, J. Appl. Phys. **84**, 4204 (1998).
[48] A. Battaglia and S. U. Campisano, J. Appl. Phys. **74**, 6058 (1993).
[49] G. Carter, J. Appl. Phys. **79**, 8285 (1996).
[50] T. Henkel, V. Heera, R. Kögler, W. Skorupa, and M. Seibt, J. Appl. Phys. **82**, 5360 (1997).
[51] A. Meldrum, R. F. Haglund, Jr., L. A. Boatner, and C. W. White, Adv. Mater. (Weinheim, Ger.) **13**, 1431 (2001).
[52] D. J. Cherniak and E. B. Watson, Chem. Geol. **172**, 5 (2000).
[53] D. J. Cherniak, Chem. Geol. **110**, 177 (1993).
[54] D. J. Cherniak, W. A. Lanford, and F. J. Ryerson, Geochim. Cosmochim. Acta **55**, 1529 (1991).
[55] E. B. Watson, D. J. Cherniak, J. M. Hanchar, T. M. Harrison, and D. A. Wark, Chem. Geol. **141**, 19 (1997).
[56] R. D. Shannon, Acta Crystallogr., Sect. A: Cryst. Phys., Diffr., Theor. Gen. Crystallogr. **32**, 751 (1976).
[57] F. Corfu, Precambrian Res. **36**, 259 (1987).
[58] J. M. Hanchar, R. J. Finch, P. W. O. Hoskin, E. B. Watson, D. J. Cherniak, and A. N. Mariano, Am. Mineral. **86**, 667 (2001).
[59] L. Nasdala, R. T. Pidgeon, D. Wolf, and G. Irmer, Mineral. Petrol. **62**, 1 (1998).